JES Focus Issue on 4D Materials and Systems

Replication and Thermal Properties of One-Dimensional Composite Nanostructures with Enhanced Mechanical Robustness

Paritat Muanchan,[1,*] Takashi Kurose,[2,] and Hiroshi Ito[1,2,**,z]**

[1] *Graduate School of Organic Materials Science, Yamagata University, Yonezawa, Yamagata 992-8510, Japan*
[2] *Research Center for GREEN Materials and Advanced Processing (GMAP), Yamagata University, Yonezawa, Yamagata 992-8510, Japan*

One-dimensional (1D) composite nanostructures, or vertically aligned composite nanostructures (VACNs), of polystyrene (PS) and graphene nanoplatelets (GNPs) (1.0-5.0 wt%) were precisely replicated by thermal nanoimprint with an anodic aluminum oxide (AAO) template. In this study, we fabricated VACNs of PS-GNPs (1.0-5.0 wt%) with a diameter of 100 nm and length of 10-70 μm, depending on the imprinting conditions. The obtained PS-GNPs 5.0 wt% VACNs showed enhancement of flat film water contact angle increasing from 87±3° to 132±2°. The nanostructures of PS-GNPs exhibit improved surface mechanical properties when compared with the neat PS. The evaluated surface mechanical properties included friction coefficient, surface durability, surface modulus, and hardness. The glass transition temperature (T_g) of PS-GNPs nanostructures increased about 1 to 4°C as compared with their bulk composites because of the immobilization the polymer chain owing to confinement in the AAO template and also due to the surface interfacial interaction effects between PS and GNPs. Moreover, the maximum thermal conduction of 1D PS-GNPs 5.0 wt% nanostructures were obtained with a value up to 1.8 W/m.K due to the control of filler orientation. The PS-GNPs nanostructures showed a higher thermal stability than that the PS nanostructures.

 [DOI: 10.1149/2.0391909jes]

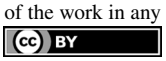

Manuscript submitted February 19, 2019; revised manuscript received May 12, 2019. Published June 5, 2019. *This paper is part of the JES Focus Issue on 4D Materials and Systems.*

Nanoengineered surfaces inspired by the nature of gecko feet and cicada wings have been produced, replicating the architecture of their nanostructures on various polymer films.[1,2] These one-dimensional (1D) nanostructures often provide multifunctional properties such as adhesiveness and hydrophobicity, and are used in biomedical applications, nanosensing materials, catalytic scaffolds, and energy storage.[3] For fabricating these nanostructures, a templating technique using anodic aluminum oxide (AAO) templates has been used combined with melt wetting and solvent wetting methods.[4–6] In particular, these wetting methods mainly focus on supramolecular chemistry such as phase separation and polymerization for materials development due to the interfacial interaction effect under nanoconfinement conditions in AAO templates.[3] However, it is still not suited to mass production because of the long process time, and also has environmental issues because of the harsh chemicals used in these methods. Therefore, development of these fabrication methods is focusing on quicker fabrication processes which are capable of being used on the industrial scale.

Over the last two decades, nanoimprint lithography has been used as a high performance and high-resolution technology for the replication of micro-/nanostructures on material surfaces.[1–7] Nanoimprint technology is very successful in both academic research and industry for fabricating ultra-fine polymeric nanostructures using AAO templates. This technique combines nanotexture and engineering design, reproducibility, high-precision manufacture with material versatility, is inexpensive, and can rapidly fabricate large areas. The use of a variety of materials with many sacrificial processes have been explored in this field. Our previous work has proposed that one-dimensional nanofiber arrays of amorphous polystyrene (PS) and semi-crystalline polypropylene (PP), with high aspect ratios of 1,000 and 2,600 respectively, can be efficiently produced by a thermal nanoimprint process using 50 nm hole-diameter AAO templates.[7] Y. Wang investigated the effect of compressed carbon dioxide (CO_2) on the enhancement of the nanoscale flowability of poly(methyl methacrylate) (PMMA) in AAO templates.[8] The results revealed that the PMMA flowability was enhanced using compressed CO_2 in the nanoimprint process. In addition, the thermoset polymer polydimethylsiloxane (PDMS) also can be used in the nanoimprinting process using AAO templates.[9] However, until now, there has been low potential for practical use of these nanostructures due to the poor on-surface mechanical stability and surface durability. To solve these problems, polymer nanocomposites using carbon materials, especially carbon nanotubes (CNTs) and graphene nanoplatelets (GNPs) have attracted much interest. It is well known that carbon material-reinforced composites exhibit excellent attributes including improved thermal, electrical, mechanical, and chemical resistance properties, which have been successfully produced using various commercialized carbon nano-filled materials.[10] Interestingly, thermal conduction and electrical conduction can be improved by control of filler orientation and polymer chain alignment based on 1D nanostructures.[11–16] Using polymer nanocomposite materials in nanoimprint processes, J. J. Hernández explored an imprinting method to replicate 1D microstructured surfaces (2.0 μm diameter) having superhydrophobic and self-cleaning properties together with enhancement in mechanical performance and electrical conductivity.[17] The model materials used were PS-CNTs and polyvinylidene fluoride (PVDF)-reduced graphene oxide (RGO) flakes and were selected to investigate use of PDMS micro replica-molds. The results demonstrated that the improvement of surface wettability was caused by the roughness of the imprinted structures. The surface mechanical properties and electrical conductivity of the polymers was enhanced by control of dispersion and orientation of the fillers in these 1D microstructures. However, imprinting at the nanoscale still has great challenges. By using the AAO nano-templating method, I. Blaszczyk-Lezak reported on how to use the wetting method to fabricate 1D composite nanostructures of PVDF with multiwall carbon nanotubes (MWCNTs).[12] The obtained composite nanostructures exhibited enhanced electrical conductivity. However, the obtained composite nanostructures still did not have good enough distribution of nanofillers due to the selective nature of infiltration in the wetting method because of the high aspect ratios and the low flowability of the MWCNTs. M. K. Smith developed an infiltration method, using AAOs with pores open only on one side, firstly filled with MWCNTs followed by the infiltration of poly(3-hexylthiophene-2,5-diyl) (P3HT), resulting in composite nanofibers being fabricated.[18] The result of the confinement induces the coalignment of MWCNTs and polymer chains. Electrical and thermal transport in the composite nanostructures improved drastically due to the increasing mass ratios of MWCNTs, where a maximum thermal

*Electrochemical Society Student Member.
**Electrochemical Society Member.
[z]E-mail: ihiroshi@yz.yamagata-u.ac.jp

Table I. Anodization conditions.

Anodization	1st	2nd
Electrical Current (A)	12.1	12.1
Applied Voltage (V)	60	60
Oxalic Acid (M)	0.3	0.3
Time (h)	17	48
Temperature (°C)	5	5

conductivity of 4.7±1.1 W/m.K was achieved with 24 wt% MWCNTs and electrical conductivity was possible once 20 wt% MWCNTs content was surpassed. However, these wetting methods still have a low replication ratio due to the flow resistance of the fluids at the nanoscale.

In this present work, 1D composite nanostructures, or vertically aligned composite nanostructures (VACNs), with high aspect ratios were precisely replicated by the thermal nanoimprint process using AAO templates. The model composite material PS-GNPs was used. Several surface properties were experimentally evaluated, consisting of wettability, friction coefficient, surface durability, surface modulus, and surface hardness.

Experimental

Materials.—Commercial grade PS (glass transition temperature (T_g) = 87°C, melt flow rate (MFR) = 18.0 g/10 min at 200°C, GPPS 679; PS Japan Corp.) and GNPs (6-8 nm-thickness, G0499; Tokyo Chemical Industry Co., Ltd.) were used in this experiment.

Preparation of AAO.—High-purity aluminum (Al) sheets (99.99%) were degreased in acetone. They were then polished in a mixed solution of $HClO_4$:H_2O:EtOH (10.0:7.0:83.0 wt%). Electropolished aluminum sheets were anodized using two-step anodization, detailed in Table I. The anodization was performed individually at a constant voltage of 60 V in 0.3 M oxalic acid, at a constant temperature of 5°C. After finishing the first anodization, the porous alumina was dissolved in a solution containing H_3PO_4 and H_2CrO_4 at 60°C. Then, the second anodization was performed. The nanopores were then opened by immersion in 5.0 wt% of the H_3PO_4 solution at 40°C on the side on which the second anodization was done.

Preparation of polymer nanocomposites.—In this study, the solution mixing method was selected to prepare the composite PS-GNPs.[19] First, GNPs were filtered by a polycarbonate (PC) membrane with 100 nm pore diameter (See Figure 1). PS pellets were dissolved in dimethylformamide (DMF) solvent with stirring at 300 rpm for 2 h. The desired amount of filtered GNPs were dispersed in a DMF solution (0.1 g of GNPs/100 mL of DMF) using ultrasonication (Branson 1200; Yamato). The GNPs/DMF solution was sonicated for 1.5 h. The sonicated GNPs/DMF solution was then added to the PS/DMF solution and then stirred at 300 rpm for 2 h. The PS-GNPs-DMF solution was dropped into a large volume of methanol to coagulate the PS/GNPs composites. The obtained PS-GNPs composites were filtered and dried in an oven at 70°C for 24 h. In this study, PS-GNPs 1.0-5.0 wt% were prepared.

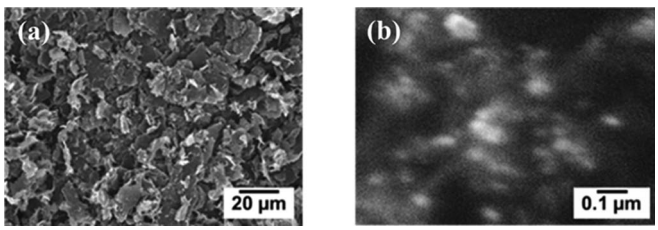

Figure 1. SEM images of GNPs (a) before filtration and (b) after filtration.

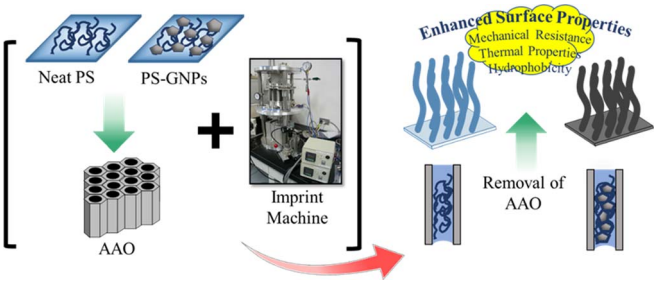

Figure 2. Fabrication of nanostructures using thermal nanoimprint process.

Preparation of polymer films.—PS or PS-GNPs pellets were melted to a thickness of 500 μm for 5 min at 200°C, followed by compression at 10 MPa in a hot press machine with a vacuum system (IMC-11FA; Imoto Machinery Co. Ltd.). The molten film was inserted into a cold press machine (IMC-181B; Imoto Machinery Co. Ltd.) for 3 min at 5 MPa.

Fabrication of nanostructures by thermal nanoimprint.—The 1D polymer nanostructure arrays were fabricated by a thermal nanoimprinting machine (Izumi Tech., Japan) using AAO templates. The experimental procedure is shown in Figure 2. The polymer films were placed on the AAO template and inserted into the thermal nanoimprint machine. The imprinting conditions are presented in Table II. After imprinting, the AAO template was removed by dissolution in 4.0 M NaOH solution for 24 h, followed by cleaning with water and drying.

Characterization.—The surface morphologies of the AAO templates and polymer nanostructures were evaluated using scanning electron microscopy (SEM, JSM-6510; JEOL Corp.) and field emission scanning electron microscopy (FE-SEM, SU-8000; Hitachi High-Technologies Corp.). A commercial contact angle meter (DM 500; Kyowa Interface Science Co. Ltd.) was used to measure the surface interaction between molten polymers/AAO surfaces and water droplets/polymer surfaces. The surface chemical property of polymer and polymer nanocomposite films were analyzed by using attenuated total reflection (ATR), IR Affinity-1s & Automatic Infrared Microscope (AIM-8800; Shimadzu Corp.). The mass ratios of GNPs in the imprinted nanostructures and their thermal stability were evaluated by thermal gravimetric analysis (TGA, TGA Q50; TA Instruments Inc.). The friction coefficient was evaluated by using a friction and wear tester (EFM-III-F; Orientec Co., Ltd.). The friction test conditions used was an applied force of 21-40 N with a rotational speed of 10 rpm for 30 s. All of the tests were performed under ambient conditions (25°C, relative humidity 35%). The surface mechanical properties at the nanoscale were also evaluated using an Agilent nanoindenter (G200; Agilent Technologies Inc.). The change in T_g of polymers and polymer nanocomposites was analyzed using modulated differential scanning calorimetry (M-DSC, DSC Q200; TA Instruments Inc.).

Thermal conductivity (κ) was estimated using the following equation

$$\kappa = \alpha \rho C_P \quad [1]$$

where α is thermal diffusivity (measured by ai-Phase Mobile 1; ai-Phase Co., Ltd.), ρ is density (measured by specific gravity

Table II. Imprinting conditions.

Materials	Temperature (°C) + Melting (5 min)	Pressure (MPa)	Press Time (min)
PS	120−180	5.0	30
PS-GNPs 1.0-5.0 wt%	120−180	5.0	30

measurement kit AD-1653 (A&D Co., Ltd.)), and C_p is the specific heat capacity (from the DSC results).[20]

Thermal conduction of the 1D nanostructures was estimated using the Effective Medium Theory (EMT), shown in Equation 2. Thermal diffusivity was measured using the templated composite films (PS-GNPs-AAO composite films) without the residual polymer layers (See Figure 3). The residual layers of the composite materials and AAO were removed after imprinting using solvent brushing with DMF (removal of remaining polymer composites, upper side) and with NaOH 4.0 M brushing (removal of the residual AAO, bottom side) followed by drying. Thermal conduction of the 1D composite nanostructures ($\kappa_{PS-GNPs(NA)}$) without the residual layers was estimated using Equation 2

$$\kappa_{PS-GNPs-AAO} = x\kappa_{PS-GNPs(NA)} + (1-x)\kappa_{AAO} \quad [2]$$

where $\kappa_{PS-GNPs-AAO}$, κ_{AAO} are the overall thermal conductivity of the PS-GNPs confined in the AAO and the skeleton of the AAO respectively, and x is the porosity.

From Equation 2, it is necessary to estimate the thermal conductivity of the AAO skeleton. B. Abad and our experimental results revealed that thermal conductivity of AAO templates is a function of the pore diameter and porosity.[21] The thermal conduction of the AAO skeleton can be estimated. Therefore, we can estimate the thermal conductivity of a single 1D nanostructure. In this study, the thermal conduction of the AAO skeleton is 1.35 W/m.K (See Figure 3).

Results and Discussion

Preparation of AAO.—The appearance of the AAO template is shown in Figure 4a. As seen in the SEM image of Figure 4b, the AAO template consists of a dense array of cylindrical nanopores, displaying abundant, highly-ordered hexagonally-packed porous cavities formed by the two-step anodization process. A narrow AAO pore size distribution can be obtained using this method. An AAO template with 100 nm pore diameter, 80 nm inter-pore distance, and 130 μm depth was prepared. Figure 4c shows a cross-sectional side view of the 100 nm diameter AAO nanocavities. The SEM micrograph in Figure 4c shows the straight sides of the the AAO pores in the prepared anodized templates. The sides of the pores are almost perfectly smooth and the pore diameter is unchanged through the depth of the AAO template.

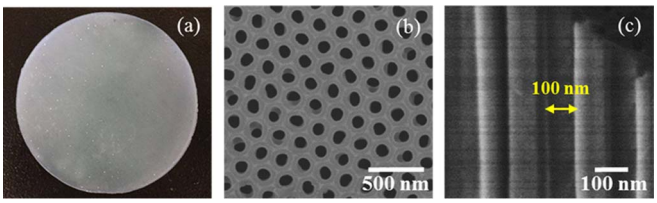

Figure 4. AAO template characteristics.

Fabrication of nanostructures by thermal nanoimprint.—To investigate the fabrication of 1D nanostructures using thermal nanoimprinting with AAO templates, the flowability of materials used at the nanoscale must be clarified. Representative SEM images (side view) of PS-GNPs 5.0 wt% VACNs obtained by thermal nanoimprinting using AAO templates are shown in Figure 5b. In Figure 5a, PS VANs and PS-GNPs (1.0-5.0 wt%) VACNs of 10-70 μm length were fabricated under our experimental conditions. The obtained bundle-form nanostructures exhibit orderly array structures, but with a tendency to agglomerate. The appearance of agglomerated nanostructures is explained by the surface adhesion induced between individual nanostructures. The results revealed that the flowability of polymer and polymer composites was enhanced by increasing the imprinting temperature, due to the reduction of intrinsic viscosity and surface energy of the polymer in the AAO templates. However, the flowability reduced with increase in the mass ratios of GNPs. The increase in the mass ratios of GNPs induced flow resistance for PS in the AAO nanochannel because of the filler-matrix interaction between GNPs and PS. An additional

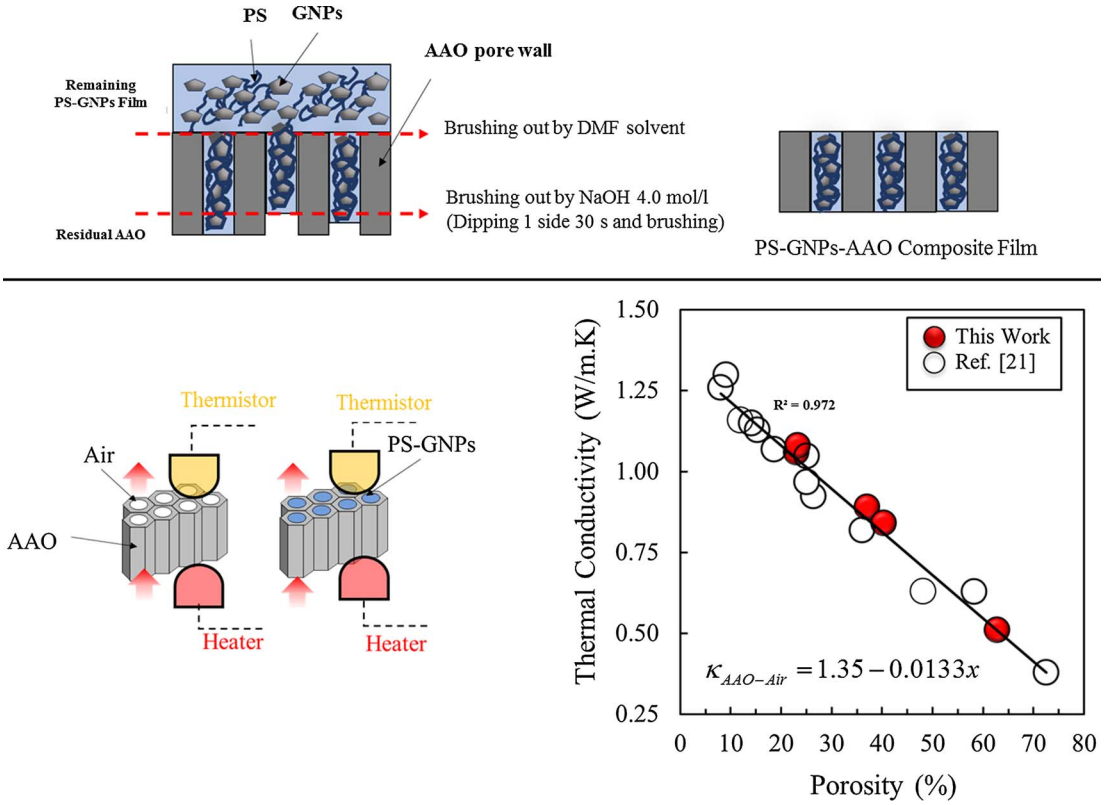

Figure 3. Preparation of PS-GNPs-AAO composite films (upper) and measurement of thermal conduction of the AAO templates (lower).

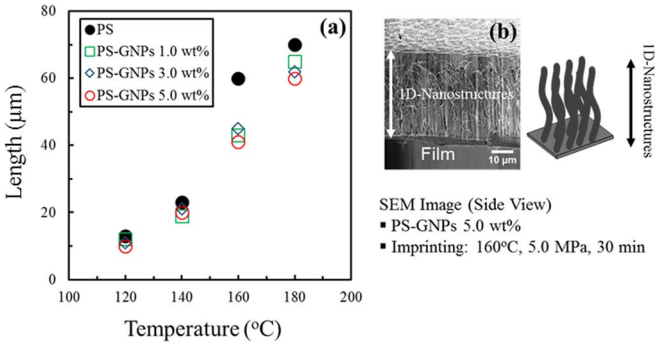

Figure 5. Nanostructures length; (a) flow displacement of polymers in AAO template and (b) SEM image of PS-GNPs nanostructures.

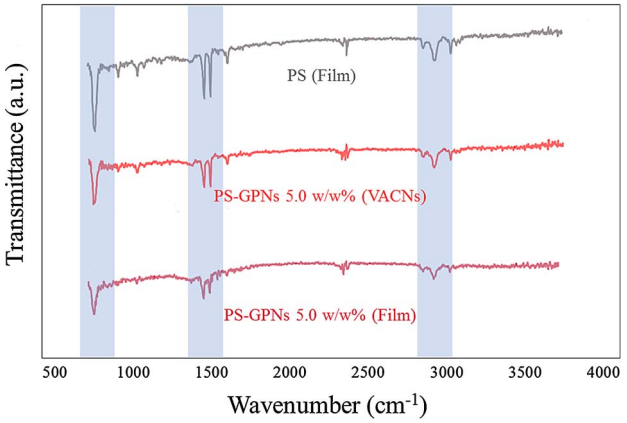

Figure 7. IR spectra of the polymer surfaces.

factor in the flow resistance is caused by the shape and dispersion of the nanoplatelets. It was found that T_g of PS was increased with increasing mass ratio of GNPs as will be discussed in next topic. The molecular orientation of PS changed because of the confinement effect and surface attraction, so restricting PS chain mobility.[22–25] It was found that the alignment of nanostructures obtained from PS-GNPs 5.0 wt% showed vertically aligned nanopillars at low imprinting temperatures (120 and 140°C). However, the vertical nanopillars became curled at high imprinting temperatures (160 and 180°C) owing to gravity becoming the dominant effect.

Our previous work has demonstrated that the flowability of molten polymers is related to the surface interaction between the polymer melt droplet and the AAO film, and can be inferred by contact angle measurement.[7] A lower contact angle indicates the interfacial resistance between the molten polymers and AAO is low. Hence, the polymers in the AAO templates can flow with lower initial imprinting conditions, such as lower imprinting temperature and pressure, and shorter imprinting time. In this present work, we measured the dynamic contact angles of the molten PS and PS-GNPs 5.0 wt% droplets on AAO surfaces at temperatures between 120-180°C. It was found that the addition of GNPs resulted in the polymer melt droplet angles increasing (See Figure 6). The contact angles of PS-GNPs 5.0 wt% droplets showed higher values than the neat PS for all melting temperatures (See Figure 6). The addition of GNPs might not only affect the flowability but also the surface energy of the materials. Moreover, the contact angle of polymer melt droplets at 180°C displayed oxophilicity, having AAO contact angles lower than 90°.

The flowability at the nanoscale of the molten polymers in the AAO imprinting process is in agreement with the Hagen-Poiseuille expression, as shown below.[13,26]

$$H = 2r\sqrt{\frac{\left(P + \frac{2\gamma\cos\theta}{r}\right)t}{32\eta}} \quad [3]$$

This equation reveals that the parameters of flowability at the nanoscale are closely related to the imprinting pressure (P), radius of the nanochannel (r), surface tension of the molten polymer (γ), contact angle of the polymer and AAO pore wall (θ), viscosity of the molten polymer (η), and infiltration time (t).The reduced viscosity of the polymer is the result of shear rate, wall slip, and the pressure used in the imprinting process. The length scale (H) was referred in the microscale-length (μm) herein.

Surface chemical analysis.—In this study, the surface chemical properties of the nanotextured material were analyzed using the FTIR method to confirm the presence of GNPs on the obtained nanostructure surfaces. The presence of GNPs confirmed the composite 1D nanostructures could be produced.[17] Figure 7 shows the IR spectrum of PS and PS-GNPs 5.0 wt% films and their obtained nanostructures. The presence of GNPs was shown by the reduction of 3 peak point intensities (753, 1451-1493 and 2991-3023 cm^{-1}) at the grayscale line in IR spectrum, so indicating the GNPs appeared on the PS nanostructure surfaces. These three spectral points are associated with the characteristic peaks of benzene rings in the PS skeleton.[27–29] Additionally, TGA was used to measure the GNPs mass ratios in the imprinted nanostructures. The TGA results will be discussed in the next later (See Figure 13).

Surface wetting properties.—The surface wettability of materials was characterized using water contact angle measurements as seen in Figure 8. A water droplet of 4 μL was dropped on the surface and the static contact angle was measured on the material surface. Imprinted nanostructures with approximately equal length between the neat PS and PS-GNPs 5.0 wt% (20±5 μm, imprinting temperature

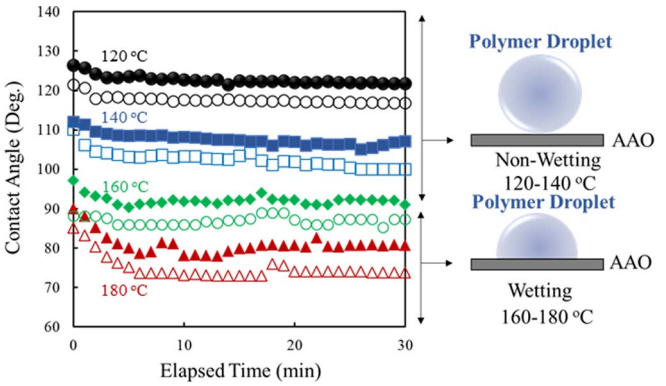

Figure 6. Polymer melt droplet angles on AAO surface (PS: hollow symbols, PS-GNPs 5.0 wt%: solid symbols).

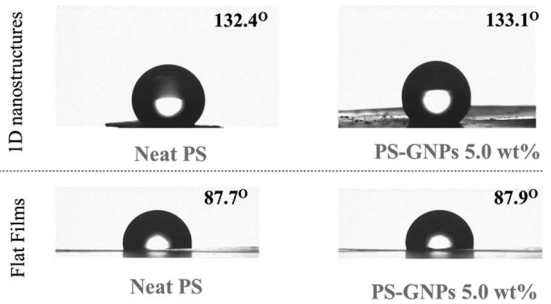

Figure 8. Polymer surface water droplet angles.

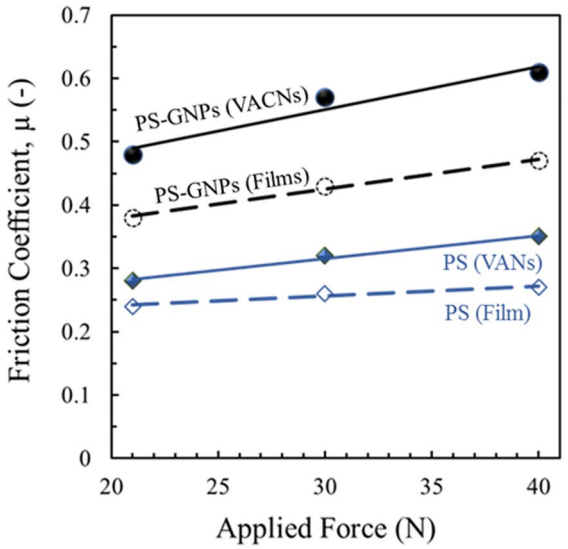

Figure 9. Friction coefficient.

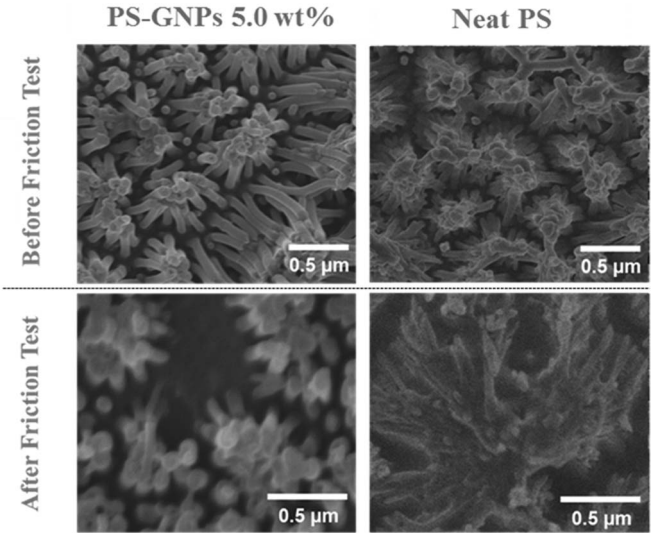

Figure 10. Nanostructure surface durability.

140°C) were used to measure the water droplet angle. Figure 8 shows the water droplets on the flat films and imprinted nanostructures for both neat PS and PS-GNPs 5.0 wt%. For the flat films, droplet angles of 87.7° and 87.9° on PS and PS-GNPs materials were observed, respectively. The nanostructure surfaces showed an increase in the water droplet angles with values of 132.4° and 133.1° for the neat PS and PS-GNPs, respectively. These results suggest that the physical roughness (r) of the materials is the dominant effect in the improvement of the hydrophobic property. The results also indicated the presence of a low GNP content of 5.0 wt% or less has no significant effect on the interfacial surface tension between the water and composite materials also the similar surface roughness ($r_{PS} = 1.77$, $r_{PS-GNPs} = 1.73$).[30] The relationship between the characteristics of the nanostructures on the physical roughness (r) can be explained by Equation 4 as follows

$$r = 1 + \frac{2\pi bh}{p^2} \quad [4]$$

where b, h and p are pillar radius, height, and pitch of the nanostructures, respectively.[17]

Surface mechanical properties.—Surface mechanical properties evaluated were friction coefficient, surface durability, hardness, and modulus. A friction and wear tester was used to measure the friction coefficient and durability of the imprinted surfaces. The hardness and modulus of the nanostructures could be obtained using a nanoindentation test. The nanoindentation technique has been shown to be suitable characterization method of nanotextured surfaces.[17, 31]

Figure 9 shows the friction coefficient of the material surfaces. The flat surfaces display relatively low friction coefficients between 0.24-0.27 for neat PS and 0.38-0.47 for PS-GNPs 5.0 wt%, while the nanotextured surfaces show higher values than those flat films with 0.28-0.35 for neat PS and 0.48-0.61 for PS-GNPs 5.0 wt%, respectively. These results reveal that the nanostructures on the material surfaces can enhance the physical roughness, resulting in an increase in the friction coefficient of the surfaces.[32–34] The replicated nanostructures enable enhanced energy dissipation through molecular plowing, causing an increase in the friction coefficient.[35] Additionally, the increase in the friction coefficient is strongly dependent on the addition of the GNPs. The reinforcement by the GNPs enhances the material stiffness, resulting in an increase in the surface mechanical resistance (drag force between the composite materials and friction test material).[36,37] Moreover, the adhesion between the surfaces might be enhanced with the increase in the nanoscale roughness due to the addition of GNPs on the PS surfaces.[38,39]

The surface durability after the friction test (40 N) was evaluated using the SEM. Figure 10 shows SEM images (top view) of the nanostructure surfaces of neat PS and PS-GNPs 5.0 wt% both before and after the friction test. In Figure 10 (right), the destruction of the nanostructure of the neat PS after friction test is seen. The vertically aligned nanostructures of the neat PS was randomized in the horizontal direction owing to the applied force during the friction test. In contrast, the nanostructure of PS-GNPs still has vertical alignment because of the improvement of the polymer mechanical resistance from the reinforcement material.[40,41] However, a few broken nanostructures were found (less than 5%) due to brittle fracture of the composite material.

The modulus and hardness of the nanostructures were evaluated using a nanoindentation test. Figure 11 shows the relationship between the mass ratios of the GNPs and the surface mechanical properties. The modulus and hardness of the nanostructures were increased respectively up to 11 and 4 folds due to the addition of the 5.0 wt% GNPs. These results agree well with the surface durability results mentioned above.[40,41]

Glass transition temperature.—The change in the glass transition temperature of the polymers is a result of confinement and surface interfacial interaction at the nanoscale. In this study, the effects of confinement and surface interfacial interaction are not only affected by the interaction between polymer and AAO but is also influenced by GNPs. Moreover, the confinement of polymers in nanopores of inorganic materials can provide an anchoring effect that leads to mechanical bonding, which plays a role in novel nanofabrication technologies such as the nanoimprinting process.[42] Many studies have reported on an increase in the polymer glass transition temperatures because of the surface interfacial interaction between the nanofilled composites and polymers. Figure 12 shows the effect of adding GNPs on the glass transition temperature of PS. In the case of polymer films, the glass transition temperature increased from ~87.1°C (neat PS) to ~97.5°C (PS-GNPs 5.0 wt%). This implies the motion of polymer chains is greatly restricted by the addition of GNPs.[43,44]

To clarify the confinement effect in AAO templates, we investigated the different glass transition temperature between their imprinted nanostructures (VACNs and VANs) and their films [$T_{g\,(VACNs,\,VANs)}$ - $T_{g\,(film)}$]. In the case of neat PS, there is no difference between $T_{g\,(VANs)}$ and $T_{g(film)}$. However, a gap between $T_{g(VACNs)}$ - $T_{g(film)}$ of up to +4°C was found with increase in GNP mass ratios to 5.0 wt%. The increases in $T_{g(VACNs)}$ - $T_{g(film)}$ due to the confinement and surface interfacial interaction effects were caused by the increasing mass ratios of GNPs and became a dominant effect. The polymer chain mobility was not only restricted by the GNPs, but also caused by the imprinting pressure and

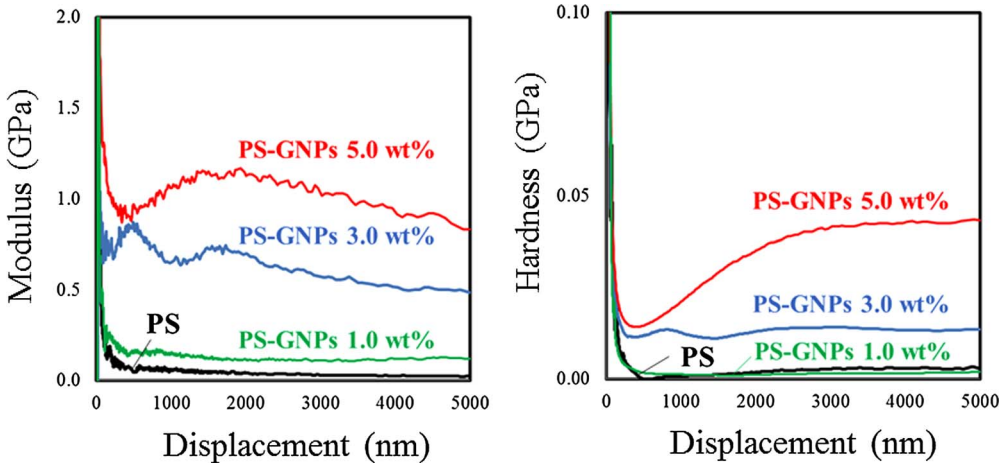

Figure 11. Nanoindentation test results.

the high mass ratio of GNPs. Moreover, the polymer chains were not stretched in the flow direction, but were squeezed in a direction orthogonal to the flow due to confinement under imprinting pressure.[45] Another report on the increase in $T_{g\,(VACNs)}$ - $T_{g\,(film)}$ attributes it to the rapid cooling process that promotes the restriction of the polymer chains at the AAO pore walls.[46]

Thermal conductivity and its stability.—In the field of polymer nanocomposites, GNPs are widely used to improve electrical conduction, thermal conduction, and mechanical properties. In this section, we investigate the thermal conduction of the polymer nanostructures.

Figure 13 shows the thermal conductivity of the neat PS and PS-GNPs 5.0 wt% for 2D films and 1D nanostructures. Thermal conduction results in the 2D and 1D nanostructures show enhancement of thermal conductivity due to the increase in the mass ratio of GNPs.[47–49] In the case of neat PS, 1D nanostructures show higher thermal conductivity than the 2D film. The reduction in dimensionality close to a single chain can limit the number of phonon scatterings, resulting in longer phonon mean free paths and higher thermal conductivity. For the 2D materials, the heat transfer is ineffective in the perpendicular direction (out-plane), causing a reduction in thermal conductivity. In general, heat is transferred more easily along the chains than in the transverse direction. Hence, the thermal conductivity can be significantly higher in the direction in which polymer chains are preferentially oriented.[20] The confinement behavior caused by the imprinting pressure may also affect the molecular orientation, polymer chain distances, and thermal capacity of the polymers, which promotes thermal conductivity in the 1D nanostructures. With the PS-GNPs material, the increase in thermal conduction of the 1D nanostructures is related to the increase in mass ratios of the GNPs. The enhancement of thermal conductivity in the composite 1D nanostructures was enhanced by the filler orientation being controlled to be parallel with the heat flux (in-plane), resulting in the thermal conductivity becoming higher.[20] The dispersion and orientation of GNPs in 1D structures was induced by a shearing effect during the imprinting process.[20] The results suggest that the thermal conduction of PS can be enhanced from 0.14 W/m.K (2D) to 1.8 W/m.K (1D, PS-GNPs 5.0 wt%).

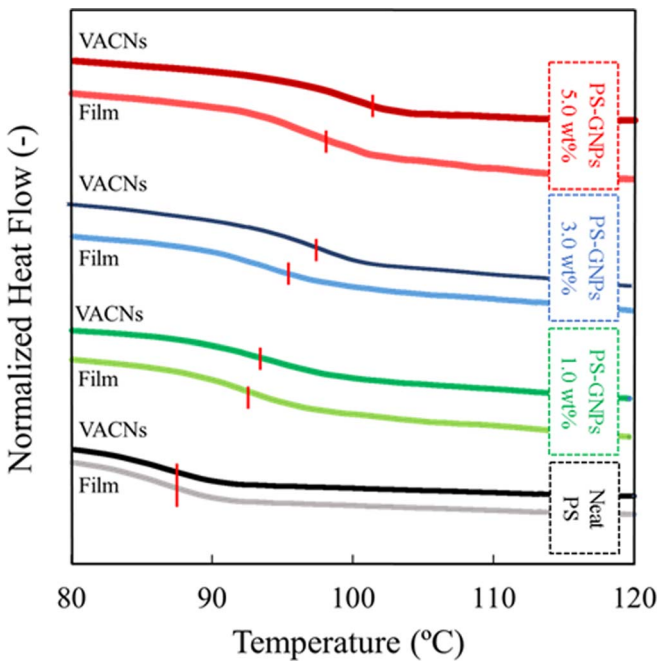

Figure 12. Glass transition temperature.

Thermal stability and mass ratios of GNPs in the VACNs were evaluated using TGA under N_2 atmosphere (See Figure 14). It was found that the thermal stability of PS improved with addition of the 5.0 wt% GNPs.[25] The mass ratio of GNPs remained in the 1D nanostructures (3.1 wt%) was smaller than that in the composite film (5.0 wt%, before imprinting) due to dispersion and geometry of the GNPs that leads to imperfect flow through the AAO templates.

Furthermore, we investigated the effects of the replication methods on the thermal conduction and thermal stability of the 1D nanostructures. The replication methods employed in this study were the thermal nanoimprint and thermal melt wetting methods. The results show the VACNs fabricated by the imprinting method have higher thermal conduction than those fabricated using the melt wetting method (See Figure 13). The superior thermal conduction is due to the GNPs being effectively driven by the imprinting pressure, resulting in a higher final mass ratio. The TGA result confirms that the mass ratio of GNPs in the nanostructures fabricated by the imprinting method is higher than in the melt wetting method (See Figure 14). Moreover, the TGA result also shows the thermal stability of the composite nanostructures fabricated by the imprinting method is higher than by the melt wetting method.

Conclusions

VACNs of PS-GNPs were fabricated using thermal nanoimprinting and AAO templates. 1D nanostructures with 100 nm diameter and 10-70 μm length can be produced depending upon imprinting conditions and the mass ratio of GNPs. The replicated nanostructures can enhance water droplet angles on the surfaces of the polymer and polymer nanocomposites owing to the increase of the physical roughness.

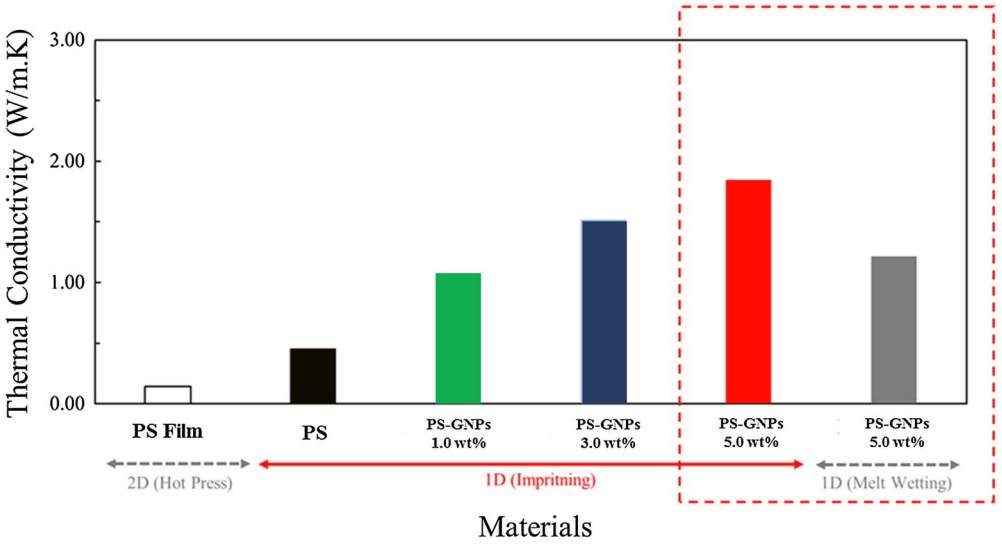

Figure 13. Polymer thermal conductivities.

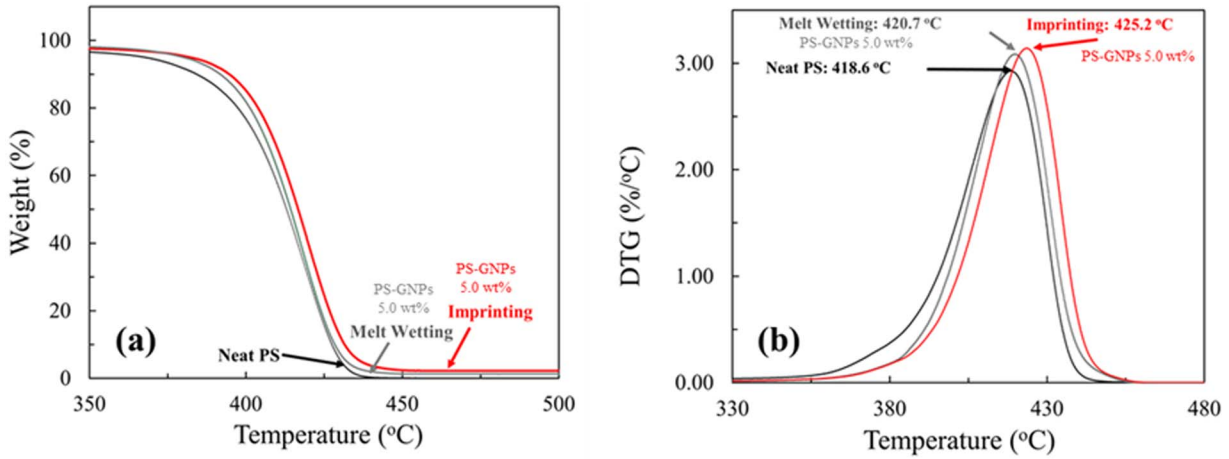

Figure 14. TGA curves of polymer films and polymer nanostructures.

The water droplet angles on the flat film surfaces of PS and PS-GNPs 5.0 wt% were 87.7° and 87.9°, respectively. In the case of 1D nanostructure surfaces, the water droplet angles were 132.4° and 133.1° for PS and PS-GNPs, respectively. Mechanical properties of the 1D nanostructures, comprising the friction coefficient, surface durability, surface modulus, and surface hardness, can be significantly enhanced by the addition of GNPs. The effects of confinement at the nanoscale and the surface interfacial interaction between PS-GNPs-AAOs result in an increase in the glass transition temperature of the composite nanostructures. The control of filler orientation in the 1D nanostructures enhances thermal conduction and thermal stability.

Acknowledgments

The authors gratefully acknowledge the support of the Japan Government (MEXT) and the Japan Society for the Promotion of Science (JSPS) in cooperation with the Innovative Flex Course for Frontier Organic Material Systems (iFront) of Yamagata University to promote full doctoral scholarship for Paritat Muanchan. This research was financially supported by JSPS Grant−in−Aid for Scientific Research (C), project ID 16K06740.

ORCID

Paritat Muanchan https://orcid.org/0000-0001-7859-9146

References

1. E. Zhang, Y. Liu, J. Yu, T. Lv, and L. Li, *J. Mater. Chem. B*, **3**, 6571 (2015).
2. H. Xie, H. X. Huang, and Y. J. Peng, *Nanoscale*, **9**, 11951 (2017).
3. C. Mijangos, R. Hernández, and J. Martín, *Prog. Polym. Sci.*,54, 148 (2016).
4. S. Ali, W. Tian, N. Ali, L. Shi, J. Kong, and N. Ali, *RSC Adv.*, **5**, 7160 (2015).
5. K. L. Yung, J. Kong, and Y. Xu, *Polymer*, **48**, 7645 (2007).
6. L. B. Huang, Y. Zhou, S. T. Han, Y. Yan, L. Zhou, and V. A. L. Roy, *Nanoscale*, **6**, 11013 (2014).
7. P. Muanchan, S. Suzuki, T. Kyotani, and H. Ito, *Polym. Eng. Sci.*, **52**, 214 (2017).
8. Y. Wang, Z. Liu, B. Han, Y. Huang, J. Zhang, D. Sun, and J. Du, *J. Phys. Chem. B*, **109**, 12376 (2005).
9. S. Lee, S. Lee, and D. Choi, *J. Korean Phys. Soc.*, **62**, L373 (2013).
10. S. K. Kumar, *Macromolecules*, **50**, 714 (2017).
11. V. Singh, T. L. Bougher, A. Weathers, Y. Cai, K. Bi, M. T. Pettes, S. A. McMenamin, W. Lv, D. P. Resler, T. R. Gattuso, D. H. Altman, K. H. Sandhage, L. Shi, A. Henry, and B. A. Cola, *Nat. Nanotech.*, **9**, 384 (2014).
12. I. Blaszczyk-Lezak, V. Desmaret, and C. Mijangos, *Express Polym. Lett*, **10**, 259 (2016).
13. A. Henry, G. Chen, S. J. Plimpton, and A. Thompson, *Phys. Rev. B.*, **82**, 144308 (2010).
14. A. Gamero-Quijano, C. Karman, N. Vila`, G. Herzog, and A. Walcarius, *Langmuir*, **33**, 4224 (2017).
15. J. Cheng and H. Pu, *Eur. Polym. J.*, **89**, 431 (2017).

16. Y. Li, H. Porwal, Z. Huang, H. Zhang, E. Bilotti, and T. Peijs, *J. Nanomater*, 2016 **Article ID 4624976**, 1 (2016).
17. J. J. Hernández, M. A. Monclús, I. Navarro-Baena, F. Viela, J. M. Molina-Aldareguia, and I. Rodríguez, *Sci. Rep.*, **7**, 1 (2017).
18. M. K. Smith, V. Singh, K. Kalaitzidou, and B. A. Cola, *ACS Appl. Mater. Interfaces*, **8**, 14788 (2016).
19. N. Heeder, I. Chakraborty, A. Bose, and A. Shukla, *J. Dynamic Behavior Mater.*, **1**, 43 (2015).
20. H. Chen, V. V. Ginzburg, J. Yang, Y. Yang, W. Liu, Y. Huang, and L. Du, *Prog. Polym. Sci.*, **59**, 41 (2016).
21. B. Abad, J. Maiz, and M. Martin-Gonzalez, *J. Phys. Chem. C*, **120**, 5361 (2016).
22. E. Rodriguez, M. Fernandez, M. E. Muñoz, and A. Santamaria, *J. Rheol.*, **60**, 1199 (2016).
23. C. Vallés, R. J. Young, D. J. Lomax, and I. A. Kinloch, *J. Mater. Sci.*, **49**, 6311 (2014).
24. M. M. Rueda, M. C. Auscher, R. Fulchiron, T. Périé, G. Martin, P. Sonntag, and P. Cassagnau, *Prog. Polym. Sci.*, **66**, 22 (2017).
25. V. Mittal and A. U. Chaudhry, *Macromol. Mater. Eng.*, **300**, 510 (2015).
26. Z. Liu, *Nat. Commun.*, **8**, 1 (2017).
27. H. Wu, W. Zhao, H. Hu, and G. Chen, *J. Mater. Chem.*, **21**, 8626 (2011).
28. C. Chen, R. Li, L. Xu, and D. Yan, *RSC Adv.*, **4**, 17393 (2014).
29. N. Wu, X. She, D. Yang, X. Wu, F. Su, and Y. Chen, *J. Mater. Chem.*, **22**, 17254 (2012).
30. F. Leroy, *Langmuir*, **29**, 1457 (2013).
31. B. J. Briscoe, L. Fiori, and E. Pelillo, *J. Phys. D: Appl. Phys.*, **31**, 2395 (1998).
32. P. M. Hansson, P. M. Claesson, A. Swerin, W. H. Briscoe, J. Schoelkopf, P. A. C. Gane, and E. Thormann, *Phys. Chem. Chem. Phys.*, **15**, 17893 (2013).
33. E. Zhang, Y. Wang, T. Lv, L. Li, Z. Cheng, and Y. Liu, *Nanoscale*, **7**, 6151 (2015).
34. S. Hu, Z. Xia, and L. Dai, *Nanoscale*, **5**, 475 (2013).
35. J. C. Spear, J. P. Custer, and J. D. Batteas, *Nanoscale*, **7**, 10021 (2015).
36. M. T. Masood, E. L. Papadopoulou, J. A. Heredia-Guerrero, I. S. Bayer, A. Athanassiou, and L. Ceseracciu, *Carbon*, **123**, 26 (2017).
37. H. Kim, A. A. Abdala, and C. W. Macosko, *Macromolecules*, **43**, 6515 (2010).
38. O. Al-Jaf, A. Alswieleh, S. P. Armes, and G. J. Leggett, *Soft Matter*, **13**, 2075 (2017).
39. H. Izadi, M. Golmakani, and A. Penlidis, *Soft Matter*, **9**, 1985 (2013).
40. J. H. Oh, T. J. Ko, M. W. Moon, and C. H. Park, *RSC Adv.*, **7**, 25597 (2017).
41. H. K. Raut, S. S. Dinachali, A. Y. He, V. A. Ganesh, M. S. M. Saifullah, J. Law, and S. Ramakrishna, *Energy Environ. Sci.*, **6**, 1929 (2013).
42. C. Teng, L. Li, Y. Wang, R. Wang, W. Chen, X. Wang, and G. Xue, *J. Chem. Phys.*, **146**, 1 (2017).
43. K. H. Liao, S. Aoyama, A. A. Abdala, and C. Macosko, *Macromolecules*, **47**, 8311 (2014).
44. Y. Han, T. Wang, X. Gao, T. Li, and Q. Zhang, *Compos. Part A: Appl. Sci. Manuf.*, **84**, 336 (2016).
45. J. Chen, L. Li, D. Zhou, X. Wang, and G. Xue, *Phys. Rev. E*, **92**, 1 (2015).
46. S. Napolitano, E. Glynos, and N. B. Tito, *Rep. Prog. Phys.*, **80**, 1 (2017).
47. Q. Bai, X. Wei, J. Yang, N. Zhang, T. Huang, Y. Wang, and Z. Zhou, *Compos. Part A: Appl. Sci. Manuf.*, **96**, 89 (2017).
48. W. Park, J. Hu, L. A. Jauregui, X. Ruan, and Y. P. Chen, *Appl. Phys. Lett.*, **104**, 1 (2014).
49. M. K. Smith, V. Singh, K. Kalaitzidou, and B. A. Cola, *ACS Appl. Mater. Interfaces* **8**, 14788 (2016).